OPTICA

Highly polarized emission from organic single-crystal light-emitting devices with a polarization ratio of 176

Ming-Hui An,[1,†] **Ran Ding,**[1,2,†] **Xu-Lin Zhang,**[1,†] **Shuo-Nan Chen,**[3] **Ya-Nan Wang,**[1]
Gao-Da Ye,[1] **Qin-Cheng Zhu,**[1] **Nian-Ke Chen,**[1] **Yu Liu,**[3] **Jing Feng,**[1,5] **and Hong-Bo Sun**[1,4,6]

[1]*State Key Laboratory of Integrated Optoelectronics, College of Electronic Science and Engineering, Jilin University, Changchun 130012, China*
[2]*Department of Applied Physics, The Hong Kong Polytechnic University, Hung Hom, Hong Kong, China*
[3]*State Key Laboratory of Supermolecular Structures and Materials, Jilin University, 2699 Qianjin Street, Changchun 130012, China*
[4]*State Key Laboratory of Precision Measurement Technology and Instruments, Department of Precision Instrument, Tsinghua University, Haidian, Beijing 100084, China*
[5]*e-mail: jingfeng@jlu.edu.cn*
[6]*e-mail: hbsun@tsinghua.edu.cn*

Polarized light emission from organic light-emitting devices (OLEDs) is of considerable current interest because of their great potential in various optical and optoelectronic devices. Utilizing materials with aligned molecular orientation is a simple and promising way to realize highly polarized OLEDs; however, both the polarization ratio and efficiency are still far from the requirements for practical applications. Organic single crystals with inherent anisotropic properties induced by their long-range periodic order are ideal candidates for intrinsically polarized emission. Herein, the intrinsic polarization has been dramatically amplified by constructing a microcavity structure in organic single-crystal OLEDs to effectively couple microcavity resonance to polarized light. A high polarization ratio of 176 has been achieved from the polarized OLEDs. Moreover, highly aligned single-crystalline molecules with small tilted orientation angles to the crystal surface result in a high outcoupling efficiency for surface-emitting crystal OLEDs. A maximum luminance of 6122 cd/m² and current efficiency of 1.86 cd/A were achieved, which are among the best performances for crystal OLEDs. This work may lead to a new strategy for simultaneously enhancing the polarization ratio and efficiency of polarized OLEDs and promote their development in various optical and optoelectronic applications.   © 2022 Optical Society of America under the terms of the OSA Open Access Publishing Agreement

https://doi.org/10.1364/OPTICA.442016

1. INTRODUCTION

Polarized emission, particularly linearly polarized emission from organic light-emitting devices (OLEDs) has gained increasing interest for a variety of potential applications, such as optical information storage, ultra-sensitive photodetectors, anti-counterfeiting processes, and high-contrast OLED display and 3D display [1–5]. In the case of OLED display, a polarized anti-glare filter is usually employed to reduce glare, leading to 50% power loss of OLEDs [1]. An extra linear polarizer is required for application of unpolarized OLEDs in stereoscopic 3D display, which also results in almost 50% power loss [2,3]. The large power loss induced by the use of a filter is an obstacle to achieving high efficiency, long-term stability, and low power consumption for the OLED display. Circularly polarized luminescence (CPL) from chiral luminophores has arisen to directly generate circularly polarized light, which can reduce the energy loss from a polarized filter. However, CPL-active materials for realizing circularly polarized OLEDs remain rare at present [6,7]. On the other hand, various optical structures have been introduced into OLED structures

to realize polarized electroluminescence (EL) [8–13]. The key parameter of a polarization ratio (PR) is usually employed to characterize the performance of polarized OLEDs and can be defined as $PR = I_{TM}/I_{TE}$, where I_{TM} and I_{TE} are intensities of transverse-magnetic (TM) and transverse-electric (TE) polarized emission at the same wavelength [12]. For example, linearly polarized OLEDs with a PR of 60.8 have been obtained by integrating a metal–dielectric nanograting as a polarizer to select TM-polarized waves and simultaneously reflect TE-polarized waves [13]. However, polarized emission enabled by external optical structures suffers the disadvantages of a complex fabrication process and precise control of parameters for optical structures. In contrast, intrinsically polarized emission by using uniaxially oriented emissive materials in OLEDs, such as liquid crystalline oligomers or polymer incorporated in emissive layers, is more easily obtained. Since the pioneering discovery of linearly polarized EL emission from OLEDs by employing stretch-oriented conjugated polymers, polarized EL emission with a PR of 2.5 by utilizing ordered films of α-sexithiophene and a PR of 51 using oriented films of β-phase

poly(9,9-dioctylfluorene) have been demonstrated [11,12]. However, treatment approaches such as rubbing, stretching, or shearing of films are usually required to obtain uniaxial alignment, which possibly deteriorates the optoelectronic properties of the films. In addition, the efficiency of intrinsically polarized OLEDs is limited by the unsatisfied optoelectronic properties of uniaxially oriented materials.

Organic single crystals with anisotropic nature are promising active materials for intrinsically highly polarized OLEDs without any subsequent treatment required [14–18]. Especially, benefiting from the high fluorescence and carrier mobility of organic single crystals, high efficiency is expectable for polarized OLEDs. Recently, Ma *et al.* reported polarized photoluminescence (PL) using a uniaxially oriented molecular crystal with high single-crystalline quality [14,18]. Ding *et al.* have demonstrated intrinsically polarized EL from α, ω-bis(biphenylyl)terthiophene (BP3T) crystal OLEDs with a PR of five [15]. Although much effort has been made to realize polarized emission from organic single-crystal OLEDs, so far, their PRs are still far from the requirements for practical applications (over $30 \sim 40$) [19]. Well-defined molecular alignment is the unique feature of organic single crystals, which contributes to their higher thermal stability, carrier mobility, and quantum efficiency compared to amorphous materials. Especially, benefiting from the high fluorescence quantum efficiency and carrier mobility of organic single crystals, high performance and device efficiency are expectable for polarized OLEDs based on organic single crystals [20,21]. Polarization of the photons emitted from crystals depends on molecular alignment. The aligned molecular orientation is preferred for highly polarized emission from crystals. On the other hand, the orientation of molecular transition dipoles determined by molecular alignment has a major impact on the light outcoupling of OLEDs [22–24]. The vertical orientation of molecular transition dipoles to the crystal surface results in horizontal propagation of emitted light, which is largely trapped in forms of waveguide (WG) modes or surface plasmon-polariton (SPPs) modes. Therefore, both polarization and outcoupling of emitted light depend on molecular alignment. Recently, polycrystalline phosphorescent films have been utilized to realize high-efficiency OLEDs because of their preferred horizontal molecular dipoles [25–28]. However, in the case of an organic single crystal with uniaxial orientation and anisotropic nature, neither polarization nor outcoupling of emitted light has been fully discussed for single-crystal OLEDs, and it remains a challenge to simultaneously realize high PRs and high efficiency from single-crystal OLEDs.

In this paper, highly polarized OLEDs with high polarization and high efficiency, and without any subsequent treatment are demonstrated by employing a cyano-substituted organic single crystal [2,5-bis(4-cyanobiphenylyl-4-yl)thiophene, BP1T-CN]. The highly aligned molecular orientation of BP1T-CN single crystals results in its intrinsically polarized PL with a high PR of eight. To achieve highly polarized EL from OLEDs with BP1T-CN as the active layers, a microcavity was constructed in the OLED structure to amplify EL polarization by coupling microcavity resonance with polarized light. A high PR of 176 was obtained from BP1T-CN single-crystal OLEDs. Besides the high PR, BP1T-CN OLEDs exhibit high EL performance with a maximum luminance of 6122 cd/m^2, current efficiency of 1.86 cd/A, and external quantum efficiency (EQE) of 1.44%, which are among the best performances of single-crystal OLEDs. The efficient light

outcoupling induced by the favorable orientation of molecular transition dipoles of BP1T-CN single crystals contributes to the high EL performance.

2. RESULTS AND DISCUSSION

A. Growth and Characteristics of Single Crystals

Here, we choose BP1T-CN single crystals for the polarized OLEDs, because its highly aligned molecular orientation is beneficial to highly polarized and efficient emission from single-crystal OLEDs. Another thiophene/phenylene co-oligomer (TPCO) 2,5-bis(4-biphenylyl-4-yl)thiophene (BP1T) with similar molecular structure was employed for comparison. BP1T-CN is recognized as a derivative of BP1T with cyano groups at the molecular terminal of BP1T [29–33]. The main difference between the single crystals of BP1T-CN and BP1T is their molecular alignment, so that the influence of molecular alignment on the EL polarization and efficiency of single-crystal OLEDs can be verified. The physical vapor transport method was used for the growth of high-quality organic single crystals (see details in Methods). BP1T-CN and BP1T single crystals both exhibit slice-like morphology with large sizes in millimeter scale and controllable thicknesses of around 300 nm. Top-view photographs of BP1T-CN and BP1T single crystals obtained by a fluorescence microscope are shown in Figs. 1(a) and 1(b). Homogeneous surface emission can be observed for the BP1T-CN single crystal, while BP1T exhibits obvious self-waveguided edge emission.

X-ray diffraction (XRD) measurements were carried out to determine the crystallography of BP1T-CN and BP1T single crystals (see Supplement 1 Fig. S1). For the BP1T-CN single crystal, peaks at 10.68° and 16.00° correspond to (002) and (003) planes, which agree with the reported triclinic crystal system ($a = 3.84$Å, $b = 16.15$Å, $c = 18.02$Å, $\alpha = 111.87°, \beta = 94.27°, \gamma = 90.43°$, space group of $P - 1$) [29]. The monoclinic BP1T single crystal also presents a set of diffraction peaks with 2θ degrees of 8.17°, 12.21°, and 16.25°, which can be assigned to (004), (006), and (008) planes ($a = 7.60$Å, $b = 5.82$Å, $c = 43.95$Å, $\alpha = 90°, \beta = 93°, \gamma = 90°$, space group of $P2_1/n$) [31]. The prominent peaks suggest the preferential [001] crystallographic orientation along the out-of-plane direction for both BP1T-CN and BP1T single crystals. In addition, atomic force microscope (AFM) images and the height profiles reveal molecular-scale flatness on the crystal surface with layer-by-layer steps of about 1.67 nm for BP1T-CN and 2.19 nm for BP1T, respectively (Supplement 1 Fig. S1). The thickness of the single molecular layer can be calculated according to the Bragg equation: $2d\sin\theta = n\lambda$, $(n = 1, 2 \ldots)$, where d is the thickness of a single molecular layer, θ is half of the diffraction degree, and λ is the x-ray wavelength of 1.5406 Å. For BP1T-CN crystals, the diffraction peaks (2θ) are located at 10.68° ($n = 2$) and 16.00° (n = 3). The d can be calculated to be 1.655 nm and 1.660 nm corresponding to (002) and (003) planes. After data averaging, the d-spacing of the BP1T-CN crystal is determined to be 1.658 nm with an error bar of 0.003 nm. In the same way, the d-spacing of the BP1T crystal can be estimated to be 2.171 nm with an error bar of 0.009 nm. The obtained d-spacings of both BP1T-CN and BP1T match well with the measured values from the AFM.

The molecular alignment of these two single crystals is shown in Figs. 1(c)–1(f). The ab-plane of both BP1T and BP1T-CN single crystals is parallel to the surface of the single crystals. The
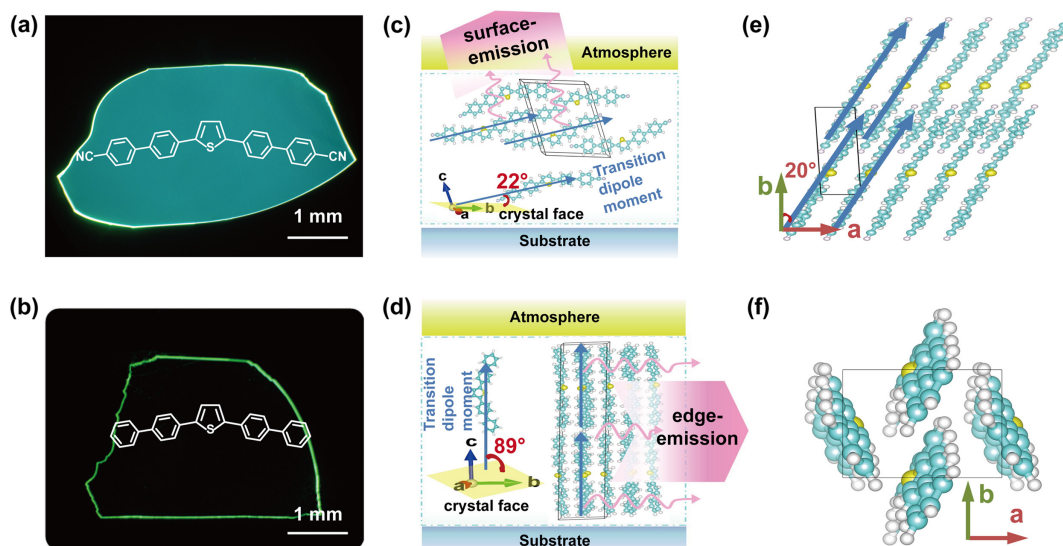
Fig. 1. Characteristics of BP1T-CN and BP1T single crystals. Top-view photographs of the (a) BP1T-CN and (b) BP1T single crystals obtained under UV light irradiation by a fluorescence optical microscope. Insets in (a) and (b) show molecular structures of BP1T-CN and BP1T, respectively. Packing motifs of (c) BP1T-CN and (d) BP1T single crystals in bc-plane. Packing motifs of (e) BP1T-CN and (f) BP1T single crystals in ab-plane.

BP1T-CN molecules are packed intertwining along the crystal a axis with a high molecular orientation to the ab-plane, while BP1T takes perfectly perpendicular molecular orientation to the crystal ab-plane. For TPCOs, the transition dipole moment between the highest occupied molecular orbital (HOMO) and lowest unoccupied molecular orbital (LUMO) is oriented parallel to the molecular long axis [29]. Therefore, the transition dipole moments of BP1T are almost perpendicular to the ab-plane with an angle of 89° to the ab-plane [Fig. 1(d)], and the angle is greatly decreased to 22° for BP1T-CN single crystals [Fig. 1(c)]. The orientation of the transition dipole moments to the crystal surface determines the direction of light emitted from the crystals, which is surface emission for BP1T-CN and edge emission for BP1T single crystals as shown in Figs. 1(a) and 1(b). On the other hand, the co-facial stacking of BP1T-CN molecules results in a highly aligned molecular orientation in the ab-plane [Fig. 1(e)], while it is typically herringbone-like molecular packing for BP1T single crystals [Fig. 1(f)]. The projection of transition dipole moments into the ab-plane for BP1T-CN is indicated in Fig. 1(e). Its orientation is defined by the angle with respect to the b axis, which is 20° for BP1T-CN, while the projection of transition dipole moments into the ab-plane is negligible for BP1T because of their upright orientation to the ab-plane with an angle of 89° [Fig. 1(f)].

B. Polarized PL Characteristics of Single Crystals

Single crystals of organic semiconductors with long-range periodic order possess intrinsic anisotropy of electrical and optical properties [12,34]. First, the non-polarized PL spectra of BP1T and BP1T-CN single crystals were measured and shown in Supplement 1 Fig. S2, which indicates the peak wavelength of 497 nm for BP1T-CN and 531 nm for BP1T single crystals, respectively. The PL of the BP1T-CN and BP1T in solution is blueshifted compared to that in single-crystal form, implying the existence of intermolecular interaction in the solid-state aggregated states (see Supplement 1 Fig. S2). Polarized PL measurements were then carried out to investigate the optical anisotropy of BP1T-CN and

BP1T single crystals. Polarized PL spectra from the single crystals were collected using an optical setup schematically illustrated in Fig. 2. As shown in Figs. 2(e) and 2(f), the excitation laser with a wavelength of 400 nm was perpendicularly incident onto the crystal ab-plane, and a linear polarizer parallel to the crystal plane was placed between the detector and crystals. Owing to their well-defined crystalline structure, transition dipole moments of BP1T-CN and BP1T molecules are in highly ordered alignment inside the crystals and lie along the molecular long axes as shown in Figs. 1(c)–1(f). By rotating the linear polarizer, the maximum intensity of the polarized PL is obtained while the polarizer lies along the molecular transition dipoles. Then, the angle of the linear polarizer can be used to determine the orientation of transition dipole moments. For BP1T-CN, the maximum and minimum intensities of polarized PL were observed while the polarizer was set parallel or perpendicular to the direction of molecular transition dipoles projected in the ab-plane, corresponding to TM and TE polarizations, respectively. In the case of the BP1T single crystal, the maximum and minimum intensities of polarized PL were observed while the polarizer was set parallel to b- or a-axis in ab-plane, corresponding to TM-polarized and TE-polarized light, respectively. TM- and TE-polarized PL spectra from BP1T-CN and BP1T single crystals are shown in Figs. 2(a) and 2(b). Figures 2(c) and 2(d) show the angle-resolved polarized PL intensity at the peak wavelength of 497 nm for BP1T-CN and 531 nm for BP1T single crystals, respectively, and the corresponding polar diagrams are shown in Supplement 1 Fig. S3. The TM-polarized PL shows a much higher intensity for BP1T-CN single crystals, and correspondingly, a much brighter TM-polarized surface emission can be observed [insets in Figs. 2(a)]. The PR for the TM to TE polarization is eight for the BP1T-CN single crystal, which is four times as high as that of BP1T with a value of two. The higher polarized PL from BP1T-CN single crystals can be attributed to its remarkable anisotropic properties induced by their highly aligned molecular orientation.
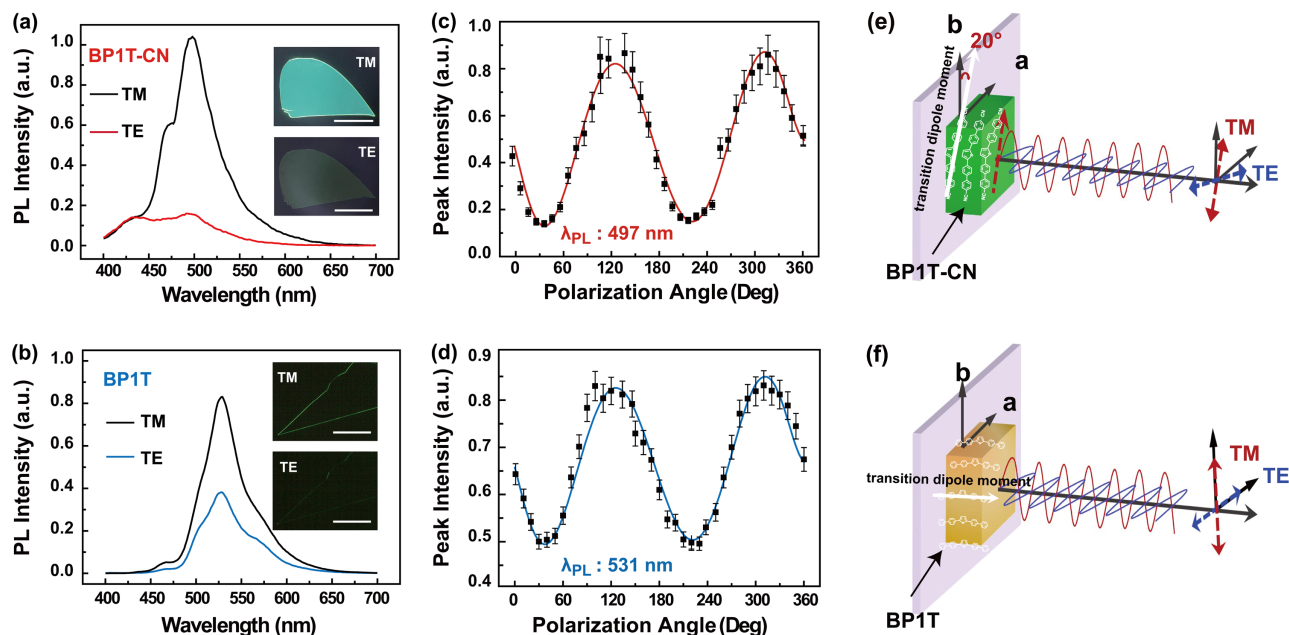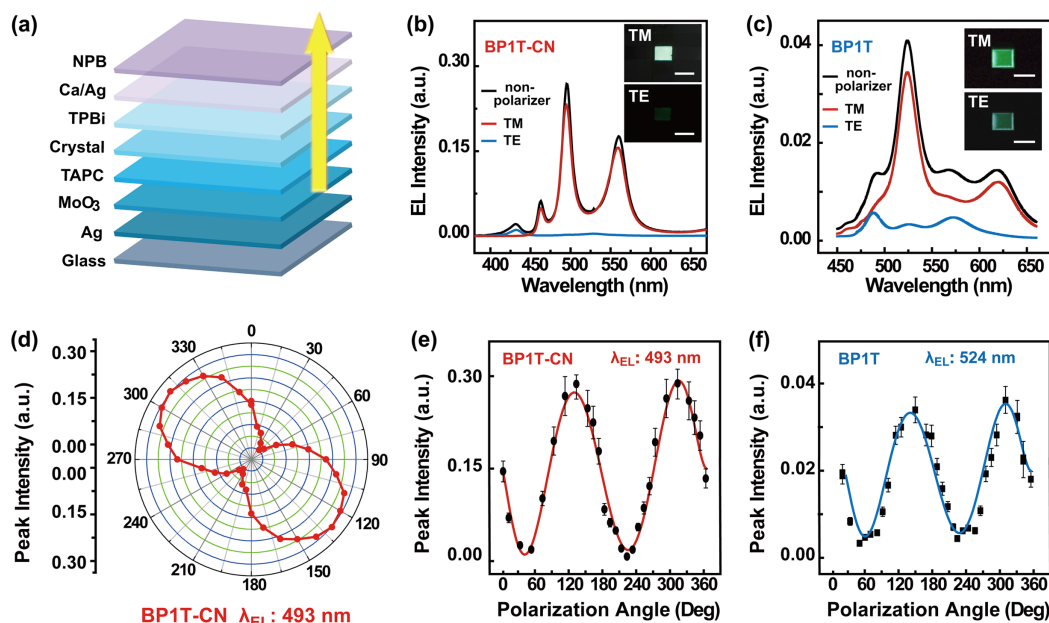
Fig. 2. Polarized PL characteristics of single crystals. Polarized PL spectra from (a) BP1T-CN and (b) BP1T single crystals. Insets in (a) and (b) show polarized fluorescence photographs of single crystals under TM and TE modes. Angle-resolved polarized PL intensity at the peak wavelength of 497 nm for (c) BP1T-CN and 531 nm for (d) BP1T single crystals. Schematic diagram of measurement setup for polarization-dependent PL and EL spectra from (e) BP1T-CN and (f) BP1T single crystals and single-crystal OLEDs.

C. Polarized EL Characteristics of Single-Crystal OLEDs

The highly polarized PL from the BP1T-CN single crystal indicates its great potential for highly polarized OLEDs. OLEDs with the BP1T-CN single crystal as the active layer were fabricated with the top-emitting structure of Ag (200 nm)/ MoO$_3$ (10 nm)/ 4, 4′-cyclohexylidenebis[N, N-bis(4-methylphenyl) benzenamine] (TAPC, 70 nm)/BP1T-CN single crystal/2, 2′2″-(1,3,5-benzinetriyl)-tris(1-phenyl-1-H-benzimidazole)   (TPBi,

70 nm)/Ca (10 nm)/Ag (20 nm)/N, N'-di-(naphthalen-1-yl)-N, N'-diphenyl-benzidine (NPB, 60 nm) [Fig. 3(a)]. Herein, MoO$_3$ as the buffer layer was employed to realize effective carrier injection and transport [35–38]; TPBi was the electron-transporting layer [39,40] and TAPC was the hole-transporting and electron-blocking layer [41]. The NPB layer deposited on the Ca/Ag cathode acts as a capping layer to enhance light transmission from the metallic electrode. OLEDs using BP1T single crystals as the active layer were fabricated with the same device structure for

Fig. 3. Polarized EL characteristics of single-crystal OLEDs. (a) Device configuration of single-crystal OLEDs with top-emitting structure. Polarized EL spectra from (b) BP1T-CN and (c) BP1T OLEDs. Insets in (b) and (c) show photographs of the operating OLEDs under TM and TE polarizations, respectively. (d) EL polar diagram of BP1T-CN OLEDs. Polarization angle-EL intensity characteristics of (e) BP1T-CN and (f) BP1T OLEDs.

comparison. The hole and electron mobilities of the BP1T-CN single crystal perpendicular to the ab-plane can be determined based on time-of-flight (TOF) measurements and calculated to be about 5.70×10^{-4} and 1.66×10^{-3} cm^2 V^{-1} s^{-1}, respectively, which are comparable to the reported hole mobility for BP1T single crystal [32]. The measured TOF transient photocurrent spectra and calculation method for the extraction of hole and electron mobility are presented in Supplement 1 Fig. S4. The polarized EL spectra and angle-resolved polarized EL intensity at the peak wavelength of 493 nm for BP1T-CN and 524 nm for BP1T single-crystal OLEDs were measured with the same setup as that of the polarized PL measurements and are shown in Figs. 3(b)–3(f). The corresponding polar diagrams of the EL intensity as a function of the polarization angle are shown in Fig. 3(d) and Supplement 1 Fig. S5. The TM-polarized EL from BP1T-CN OLEDs exhibits spectra similar to that of non-polarized EL in both intensity and the positions of the emission peaks, while the TE-polarized EL became almost extinct [Fig. 3(b)]. The PR of TM/TE for BP1T-CN OLEDs is 176 at the peak wavelength of 493 nm. The EL at the other two peak wavelengths of 464 nm and 563 nm also exhibits high PRs of 50 and 110, respectively. In contrast, BP1T OLEDs showed a much lower PR of 10 at the peak wavelength of 524 nm. Photographs of the operating OLEDs with TM and TE polarizations shown in the insets of Figs. 3(b) and 3(c) confirm the large variation of polarization performance between BP1T-CN and BP1T OLEDs. Bright TM-polarized EL and weak TE-polarized EL can be observed from BP1T-CN OLEDs, while there is no obvious difference in the EL brightness between TM and TE polarizations for BP1T OLEDs. The PL from BP1T single crystals and EL from BP1T OLEDs show comparable PRs of two and 10, respectively. However, it should be noted that the EL from BP1T-CN OLEDs with a PR of 176 is much higher than that of the PL PR of eight from BP1T-CN single crystals, which is enhanced by 22 times. Single-crystal OLEDs consisting of a reflective bottom metallic electrode and a semitransparent top metallic electrode will establish a microcavity structure [23,42–46]. The much higher polarized EL compared to PL can be attributed to the microcavity effect in single-crystal OLEDs.

To verify the microcavity effect in BP1T-CN OLEDs, angle-resolved EL spectra were measured without a linear polarizer by changing the observation angles from 0° to 60° with respect to the normal direction of the device surface. The EL emission peaks towards the short wavelengths with increasing observation angles [Supplement 1 Fig. S6(a)]. Numerical simulations were performed to interpret the experimental results. We applied a dipole model method [47] to calculate the dissipated power spectra of the device for TM- and TE-polarized light at different observation angles (see Methods). The polarized reflectance spectra of BP1T-CN and BP1T single crystals were measured to calculate their anisotropic refractive indices (Supplement 1) [48–51]. The fitting method for anisotropic refractive indices of single crystals are presented with details in Supplement 1 Fig. S7. They are 4.2 and 1.8 for BP1T-CN, along the axes parallel and perpendicular to the projection of transition dipoles in the ab-plane, respectively, and 1.6 and 1.8 for the BP1T single crystal along the a and b axes in the ab-plane. Large refractive indices beyond the value of four have been observed in TPCO crystals, which can be ascribed to their highly aligned molecular orientation in single crystals [48–51]. The measured refractive indices of BP1T crystals are in coincidence with previous reports [33]. The highly aligned molecular orientation

of BP1T-CN in the ab-plane results in its significant anisotropic properties compared to the BP1T single crystal. The resonant peaks in the calculated spectra can be attributed to the microcavity mode. The TM and TE dispersion curves obtained from angle-resolved EL measurements and calculated results by using a dipole model method are presented in Supplement 1 Fig. S6(b), where the resonant wavelengths were found to shift to blue with increasing observation angles. This is a typical feature of microcavity resonance [23,44–46]. The numerically obtained dispersion relations match well with experimental measurements, indicating that the blueshift of the EL emission as well as the appearing peaks result from the microcavity effect in single-crystal OLEDs.

D. Calculated Dissipated Power Spectra and Electric Field Intensity Distributions of Single-Crystal OLEDs

The microcavity effect plays an important role in achieving EL with a high PR from BP1T-CN OLEDs. As can be seen in Fig. 3(b), the measured EL spectra under TM and TE polarizations are different in the normal direction of BP1T-CN OLEDs. There are three microcavity resonant peaks for TM polarization but two resonances for TE polarization, and these peak wavelengths are obviously different from each other. The variation in resonant wavelengths can be attributed to the large variation in their refractive indices (4.2 and 1.8) for TM and TE polarizations. The calculated dissipated power spectra at normal angles with TM and TE polarizations for both BP1T-CN OLEDs are shown in Fig. 4(a). The resonant wavelength of microcavity modes is determined by the cavity length, which depends on the crystal thickness for crystal OLEDs. The crystal thickness is precisely chosen during device fabrication for matching the microcavity resonance with the PL emission peak. Considering the PL peak wavelengths of ∼493 and ∼524 nm for BP1T-CN and BP1T crystal, the thicknesses of BP1T-CN and BP1T were selected to be 600 nm and 690 nm in single-crystal OLEDs, respectively, for the coincidence of microcavity resonance with PL peak wavelengths of the two crystals. It is known that light emission can be highly enhanced by the Purcell effect in the microcavity structure under the resonant conditions; therefore, TM-polarized light can be efficiently emitted at the peak wavelength of 493 nm. In the case of TE polarization, no microcavity resonance is supported at the same wavelength, so that the corresponding TE-polarized light emission is greatly suppressed. Therefore, the high PR of 176 at the wavelength of 493 nm can be achieved. This high PR is also explained in Fig. 4(b) by showing the calculated TM-polarized electric field intensity distributions inside the device as a function of wavelength (horizontal axis). The three field enhancement regions correspond to three microcavity resonances at which the generated dominated TM-polarized light (see the dipoles in the inset) can be enhanced and outcoupled. The measured EL spectra and calculated dissipated power spectra at normal angles under TM and TE polarizations for BP1T OLEDs are shown in Supplement 1 Fig. S8. Although the microcavity effect also exists in BP1T OLEDs, the small variation between the refractive indices along a and b axes makes very little difference in the emission ratio of TM- and TE-polarized light and therefore a much lower PR (∼10 at the 524 nm).

To further verify the effect of the microcavity on the large PR, another single-crystal OLED with a weak cavity structure was constructed with top-emitting and inverted structure of Ag (200 nm)/Ca (10 nm)/TPBi (35 nm)/BP1T-CN or BP1T single crystal/TAPC (40 nm)/MoO$_3$ (5 nm)/Au (8 nm) [Supplement 1
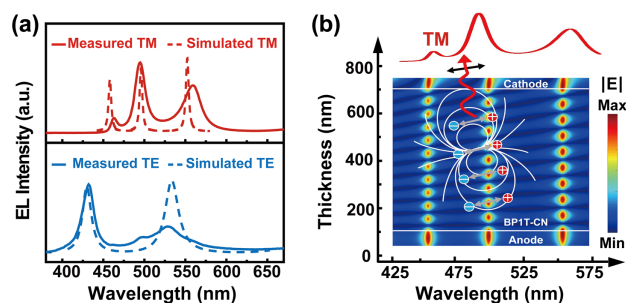
Fig. 4. (a) Measured EL spectra and calculated dissipated power spectra at normal angle with TM and TE polarizations for BP1T-CN OLEDs. (b) Calculated TM-polarized electric field intensity distributions inside BP1T-CN single-crystal OLEDs at different wavelengths.

Fig. S9(a)]. Here, the microcavity effect is very weakened by using an ultra-thin Au layer with high optical transparency of 77.4% as the top anode [52]. Figures S9(b) and (c) (see Supplement 1) show the polarization-dependent EL spectra of single-crystal OLEDs with weak cavities. We also performed numerical simulations of TM-polarized light to calculate the radiated power spectra (Supplement 1 Fig. S10). To achieve the coincidence of microcavity resonance with the PL peak wavelength of BP1T-CN, the thickness of BP1T-CN was selected to be around 525 nm in weak-microcavity BP1T-CN OLEDs. As expected, the PRs for polarized EL emission are much lower than that from strong-microcavity OLEDs, which were measured to be 20 at the wavelength of 525 nm for BP1T-CN and less than two at the wavelength of 495 nm for BP1T OLEDs [Supplement 1 Figs. S9(d), (e) and Fig. S11]. Therefore, we can conclude that both the anisotropy properties of BP1T-CN single crystals and microcavity effect of the OLED structure contribute to the high EL PR from BP1T-CN OLEDs.

In particular, the quality factor is an important parameter to judge the quality of a microcavity. It can be calculated by the equation [53] $Q = \lambda/\Delta\lambda$, where λ is the peak wavelength, and $\Delta\lambda$ is the value of full width at half maximum. The calculated Q values of these BP1T-CN OLEDs with strong microcavities are higher than those of BP1T OLEDs and BP1T-CN OLEDs with weak microcavities (Supplement 1 Table S1). These results prove directly that the huge increase in PR and EL amplification of BP1T-CN OLEDs is attributed to the high anisotropy of the BP1T-CN crystal as well as the microcavity induced Purcell effects [44–46,51].
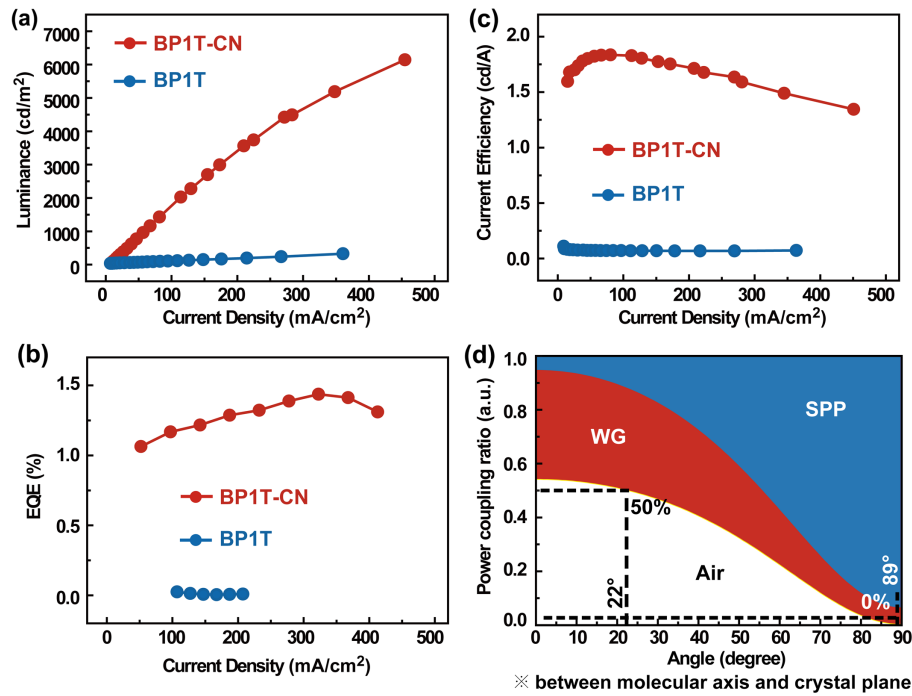
E. EL Performances of Single-Crystal OLEDs

It is known that the transition dipole orientation of emitting molecules influences the outcoupling efficiency of OLEDs. Considering the highly ordered molecular alignment of organic single crystals, the transition dipole orientation is one of the key factors to determine the EL performance of single-crystal OLEDs. The EL performance of single-crystal OLEDs based on BP1T and BP1T-CN single crystals are shown in Figs. 5(a)–5(c). The maximum luminance, current efficiency, and EQE of 6122 cd/m², 1.86 cd/A, and 1.44%, respectively, were obtained from BP1T-CN OLEDs, while they are 290 cd/m², 0.12 cd/A, and 0.2%, respectively, for BP1T OLEDs. BP1T-CN OLEDs exhibit much better EL performance than that of BP1T OLEDs with more than one order of magnitude enhancement in both brightness and current efficiency. Table 1 summarizes the EL performance of polarized OLEDs based on various emitting materials highlighting the key criteria of PR. As can be seen in Table 1, BP1T-CN crystals show great potential for realizing polarized OLEDs with high EL efficiency and high PR.

The light emitted from dipoles is trapped in single crystals in the form of WG mode or at the metallic electrode/organic interface in the form of SPPs, except that directly outcoupled to air. The power coupling ratio as a function of the dipole orientation angle for OLEDs was calculated at a non-resonant wavelength of 500 nm without loss of generality, which can verify the dependence of the outcoupling efficiency on the orientation of the emitting dipole [Fig. 5(d)]. The power coupling ratios in different channels are found to highly depend on the dipole orientation angles. This is due to the fact that most of the light emitted from transition dipoles will propagate along the direction perpendicular to that of the dipole moments. In this way, a small angle will dramatically lower the coupling efficiency to SPPs and simultaneously increase the outcoupling efficiency to air, which is obviously beneficial to device efficiency. This is exactly the case of the BP1T-CN single crystal with a tilted orientation angle of 22°, which corresponds to 50% outcoupling efficiency. In the case of the BP1T single crystal with upright molecular dipole orientations, the coupling ratio to air drops to almost zero. Therefore, the highly aligned molecular orientation with the small tilted orientation angle to the crystal surface of the BP1T-CN is a benefit to not only the high PR but also the high outcoupling efficiency of surface-emitting BP1T-CN OLEDs.

Table 1.   Comparison of EL Performance of Reported Polarized OLEDs Based on Various Emitting Materials in Different Crystalline Types

Crystalline Type	Materials	Luminance (cd/m²)	Current Efficiency (cd/A)	EQE (%)	Polarization Ratio (TM/TE)	Ref
Nano crystalline	CdSe/CdS	170	0.24	[-]	~1.5	[17]
Amorphous	PBO	[-]	[-]	[-]	1.6	[8]
Poly crystalline	αT6	[-]	[-]	0.001	2.5	[11]
Amorphous	F8BT	150	[-]	[-]	5	[4]
Single crystalline	BP3T	5	[-]	0.00024	5	[15]
Liquid crystalline	PFO	700	0.14	[-]	29	[9]
Amorphous	N-phase PFO	[-]	1	[-]	45	[12]
Liquid crystalline	β-phase PFO	[-]	2	[-]	51	[12]
Single crystalline	BP1T	290	0.12	0.2	10	This work
Single crystalline	BP1T-CN	6122	1.86	1.44	176	This work

Fig. 5. EL performances of the single-crystal OLEDs. (a) Current density-luminance, (b) current density-EQE, and (c) current density-current efficiency characteristics of OLEDs. (d) Calculated power coupling ratio as a function of dipole orientation angle.

3. METHODS

Single-crystal growth: BP1T powder was supplied by Tokyo Chemical Industry and used without any treatment. BP1T-CN was synthesized and purified according to published reports [30]. Crystal growth was carried out through the method of physical vapor transport as the following procedure. Molecular powder was first placed in a horizontal tube furnace and purged with pure Ar gas flow. The sublimation temperature, crystallization temperature, and Ar gas flow were precisely controlled for both BP1T (330°C, 290°C, and 38 ml/min) and BP1T-CN (380°C, 340°C, and 56 ml/min). By heating for about 4 h, thin plate-like crystals can be obtained at the tube wall. Crystals can be picked up using anti-static tweezers and transferred to arbitrary substrates for further measurements and device fabrication.

OLEDs fabrication: basic fabrication for single crystal-based OLEDs was described in our previously published literature [35–38]. First, we selected a grown single crystal and transferred it onto the octadecyltrichlorosilane (OTS)-treated SiO_2/Si substrates. Thereafter, the multilayers, including NPB, TPBi, and cathode (Ca/Ag) layers, were thermally deposited onto high-quality crystals at a controlled rate (1 Å/s) under a high vacuum level of 1×10^{-4} Pa. Then, a little drop of photoresist (NOA63, Norland) was dropped onto the crystal surface and flattened by a piece of glass substrate. After 15 min of exposure to UV light, thin NOA63 polymer film was cured, and then the device was peeled off from the OTS/ SiO_2/ Si substrate and transferred to a clean glass substrate. The TAPC, MoO_3, and anode (ultra-thin Au or Ag) layers were respectively deposited onto the opposite side of the crystal. The active area of completed devices was 200 μm × 300 μm.

Coupling ratio calculation: a dipole model was applied to calculate the power coupling ratio in our device as a function of the dipole orientation angle. In the model, vertical and horizontal dipoles are assumed to be located in the active layer. The outcoupled power density, namely, for vertical dipoles coupling to TM waves, is defined as K_{TMv}, while K_{TMh} and K_{TEh} are those for horizontal dipoles coupling to TM and TE waves, respectively. These power densities can be calculated via [47]

$$K_{TMv} = \frac{3}{2}\text{Re}\left[\frac{u^3}{\sqrt{1-u^2}}\frac{(1+a_{TM}^+)(1+a_{TM}^-)}{1-a_{TM}}\right],$$

$$K_{TMh} = \frac{3}{4}\text{Re}\left[\frac{u}{\sqrt{1-u^2}}\frac{(1-a_{TM}^+)(1-a_{TM}^-)}{1-a_{TM}}\right],$$

$$K_{TEh} = \frac{3}{4}\text{Re}\left[u\sqrt{1-u^2}\frac{(1+a_{TE}^+)(1+a_{TE}^-)}{1-a_{TE}}\right], \quad (1)$$

where u is related to the parallel wave vector, and a_{TM} and a_{TE} are related to the reflection coefficients on the top and bottom interfaces of the active layer, respectively. In this method, the key process is the coefficients' determination of a_{TM} and a_{TE}, which can be obtained using an anisotropic transfer matrix method. The anisotropic transfer matrix method can be employed to calculate the transmission, reflection, and absorption of light in multilayer structures.

Anisotropic transfer matrix method: a brief process is to first write the electric and magnetic fields in each layer as forward-propagating and backward-propagating waves in the exponential form. Then we use the boundary condition at each interface between two layers (i.e., the tangential components of electric and magnetic fields are continuous) to construct a matrix relation between adjacent layers. By transferring the matrix from the first layer to the last layer, we can establish a matrix to calculate the amplitudes of the electric and magnetic fields in all layers, based on the incidence in the first layer. These amplitude coefficients are

finally used to calculate the transmission, reflection, and absorption of light in this multilayer structure. In the calculation, the thickness and refractive index of each layer are needed. Since the refractive index of the crystal layer is anisotropic, this method is known as the anisotropic transfer matrix method. Here we take the strong-microcavity BP1T-CN device for example. To determine $a_{TM}^+(a_{TE}^+)$, we consider a structure: crystal/TPBi (70 nm)/Ag (20 nm)/NPB (60 nm)/Air, where the refractive index of TPBi and NPB is set to be 1.7, while that of Ag is calculated from the Drude model. To determine $a_{TM}^+(a_{TE}^+)$, on the other hand, we consider a structure: crystal/TAPC (70 nm)/Ag (80 nm)/glass, where the refractive index of TAPC is chosen as 1.7. The thickness of the crystal layer is set to be 600 nm. After obtaining these coefficients, the radiated power can simply be calculated via the sum of these contributions [47]:

$$K_{TM} = K_{TMv}\sin^2\theta + K_{TMh}\cos^2\theta, \ K_{TE} = K_{TEh}\cos^2\theta, \quad (2)$$

where θ is the tilted angle of the dipole in our device (e.g., $\theta = 22°$ for the BP1T-CN device; $\theta = 89°$ for the BP1T device).

Characterizations: optical photographs of single crystals were collected through widefield fluorescence microscopy under UV light irradiation. An x-ray diffractometer was employed to record the XRD patterns under a scanned mode from $5°$ to $20°$ (2θ) (Rigaku, D/max-rA). The surface morphology of organic single crystals was scrutinized by AFM in a tapping mode (Bruker). PL spectra were carried out using a fluorescence spectrophotometer (Hitachi, F-4600). EL characteristics of the single-crystal OLED devices were performed by a PR-788 extended dynamic range spectroradiometer with the assistance of Keithley 2400 source meters. The crystallographic data of the crystal structures were downloaded free of charge from the Cambridge Crystallographic Data Centre, CCDC, 12 Union Road, Cambridge CB21EZ, UK.

4. CONCLUSION

In summary, highly polarized and efficient single-crystal OLEDs have been demonstrated by using the single crystal of BP1T-CN with highly aligned molecular orientation as the active materials. The PR of TM/TE was dramatically increased from eight for the polarized PL emitted from BP1T-CN single crystals to 176 for the polarized EL emitted from BP1T-CN OLEDs. Both experimental results and theoretical simulations confirm that the EL polarization was amplified by coupling microcavity resonance to polarized light through precisely constructing a microcavity in the OLED structure. In addition, the highly aligned molecular orientation of BP1T-CN is beneficial to the high outcoupling efficiency of surface-emitting BP1T-CN OLEDs. Therefore, the maximum luminance of 6122 cd/m^2, current efficiency of 1.86 cd/A, and EQE of 1.44% were achieved for BP1T-CN single-crystal OLEDs. The in-depth exploration of the mechanism and optimization of polarized OLEDs based on organic single crystals paves the way for practical applications of organic single-crystalline materials in the field of organic electronics and optoelectronics.

Disclosures. The authors declare no conflicts of interest.

Data availability. Data underlying the results presented in this paper are not publicly available at this time, but may be obtained from the authors upon reasonable request.

Supplemental document. See Supplement 1 for supporting content.

†M.H.A., R.D., and X.L.Z. contributed equally to this work.

REFERENCES

1. L. Wan, J. Wade, F. Salerno, O. A. Beth Laidlaw, X. H. Wang, T. Penfold, M. J. Fuchter, and A. J. Campbell, "Inverting the handedness of circularly polarized luminescence from light-emitting polymers using film thickness," ACS Nano **13**, 8099–8105 (2019).

2. P. Boher, T. Leroux, T. Bignon, and V. C. Patton, "Multispectral polarization viewing angle analysis of circular polarized stereoscopic 3D displays," Proc. SPIE **7524**, 75240R (2010).

3. D. M. Lee, J. H. Jung, Y. J. Lee, C. J. Yu, and J. H. Kim, "Brightness enhancement of 3D display through patterning linearly polarized OLED," SID Symp. Dig. Tech. **48**, 2018–2020 (2017).

4. K. S. Whitehead, M. Grell, D. D. C. Bradley, M. Inbasekaran, and E. P. Woo, "Polarized emission from liquid crystal polymers," Synth. Met. **111**, 181–185 (2000).

5. F. Getman, M. Makarenko, A. Burguete-Lopez, and A. Fratalocchi, "Broadband vectorial ultrathin optics with experimental efficiency up to 99% in the visible region via universal approximators," Light Sci. Appl. **10**, 47 (2021).

6. S. Lee, Y. Lee, K. Kim, S. Heo, D. Y. Jeong, S. Kim, J. Cho, C. Kim, and Y. You, "Twist to boost: circumventing quantum yield and dissymmetry factor trade-off in circularly polarized luminescence," Inorg. Chem. **60**, 7738 (2021).

7. Y. J. Deng, M. Z. Wang, Y. L. Zhuang, S. J. Liu, W. Huang, and Q. Zhao, "Circularly polarized luminescence from organic micro-/nano-structure," Light Sci. Appl. **10**, 76 (2021).

8. C. C. Wu, P. Y. Tsay, H. Y. Cheng, and S. J. Bai, "Polarized luminescence and absorption of highly oriented, fully conjugated, heterocyclic aromatic rigid-rod polymer poly-p phenylenebenzobisoxazole," J. Appl. Phys. **95**, 417–423 (2004).

9. K. Sakamoto, K. Miki, M. Misaki, K. Sakaguchi, M. Chikamatsu, and R. Azumi, "Very thin photoalignment films for liquid crystalline conjugated polymers: application to polarized light-emitting diodes," Appl. Phys. Lett. **91**, 183509 (2007).

10. J. Xia, J. W. Tang, F. L. Bao, Y. C. Sun, M. D. Fang, G. J. Cao, J. L. Evans, and S. He, "Turning a hot spot into a cold spot: polarization-controlled Fano-shaped local-field responses probed by a quantum dot," Light Sci. Appl. **9**, 116 (2020).

11. R. N. Marks, F. Biscarini, R. Zamboni, and C. Taliani, "Polarized electroluminescence from vacuum grown organic light-emitting diodes," Europhys. Lett. **32**, 523–528 (1995).

12. M. Misaki, M. Chikamatsu, Y. Yoshida, R. Azumi, N. Tanigaki, K. Yase, S. Nagamatsu, and Y. Ueda, "Highly efficient polarized polymer light-emitting diodes utilizing oriented films of β-phase poly(9,9-dioctylfluorene)," Appl. Phys. Lett. **93**, 023304 (2008).

13. L. Zhou, Y. Zhou, B. L. Fan, F. Nan, G. H. Zhou, Y. Y. Fan, W. J. Zhang, and Q. D. Ou, "Tailored polarization conversion and light-energy recycling for highly linearly polarized white organic light-emitting diodes," Laser Photon. Rev. **14**, 1900341 (2020).

14. Y. P. Li, F. Z. Shen, H. Wang, F. He, Z. Q. Xie, H. Y. Zhang, Z. M. Wang, L. L. Liu, F. Li, M. Hanif, L. Ye, and Y. G. Ma, "Supramolecular network conducting the formation of uniaxially oriented molecular crystal of cyano substituted oligo(p-phenylenevinylene) and its amplified spontaneous emission (ASE) behavior," Chem. Mater. **20**, 7312–7318 (2008).

15. R. Ding, J. Feng, W. Zhou, X. L. Zhang, H. H. Fang, T. Yang, H. Y. Wang, S. Hotta, and H. B. Sun, "Intrinsic polarization and tunable color of electroluminescence from organic single crystal-based light emitting devices," Sci. Rep. **5**, 12445 (2015).

16. Y. Yamada and H. Yanagi, "Polarized blue light-emission from epitaxially oriented bis(phenyloxazolyl)benzene crystals," Appl. Phys. Lett. **76**, 3406–3408 (2000).

17. A. Rizzo, C. Nobile, M. Mazzeo, M. Giorgi, A. Fiore, L. Carbone, R. Cingolani, L. Manna, and G. Gigli, "Polarized light emitting diode by longrange nanorod self-assembling on a water surface," ACS Nano **3**, 1506–1512 (2009).

18. Y. X. Xu, H. Y. Zhang, F. Li, F. Z. Shen, H. Wang, X. J. Li, Y. Yu, and Y. G. Ma, "Supramolecular interaction-induced self-assembly of organic molecules into ultra-long tubular crystals with wave guiding and

amplified spontaneous emission," J. Mater. Chem. **22**, 1592–1597 (2012).

19. B. Park, "Polarized light-emission from photonic organic light-emitting devices," in *Book of Organic Light Emitting Devices*, J. Singh, eds. (Academic, 2012), pp. 44–64.

20. H. Liu, L. Yao, B. Li, X. Chen, Y. Gao, S. Zhang, W. Li, P. Lu, B. Yang, and Y. G. Ma, "Excimer-induced high-efficiency fluorescence due to pairwise anthracene stacking in a crystal with long lifetime," Chem. Commun. **52**, 7356 (2016).

21. M. Yamagishi, J. Takeya, Y. Tominari, and Y. Nakazaw, "High-mobility double-gate organic single-crystal transistors with organic crystal gate insulators," Appl. Phys. Lett. **90**, 182117 (2007).

22. J. Kim, T. Batagoda, J. Lee, D. Sylvinson, K. Ding, P. J. G. Saris, U. Kaipa, I. W. H. Oswald, M. A. Omary, M. E. Thompson, and S. R. Forrest, "Systematic control of the orientation of organic phosphorescent Pt complexes in thin films for increased optical outcoupling," Adv. Mater. **31**, 1900921 (2019).

23. C. X. Zang, S. H. Liu, M. X. Xu, R. F. Wang, C. Cao, Z. L. Zhu, J. M. Zhang, H. Wang, L. Zhang, W. F. Xie, and C. S. Lee, "Top-emitting thermally activated delayed fluorescence organic light-emitting devices with weak light-matter coupling," Light Sci. Appl. **10**, 116 (2021).

24. K. H. Kim, J. L. Liao, S. W. Lee, B. Sim, C. K. Moon, G. H. Lee, H. J. Kim, Y. Chi, and J. J. Kim, "Crystal organic light-emitting diodes with perfectly oriented non-doped Pt-based emitting layer," Adv. Mater. **28**, 2526–2532 (2016).

25. S. Y. Kim, W. I. Jeong, C. Mayr, Y. S. Park, K. H. Kim, J. H. Lee, C. K. Moon, W. Brütting, and J. J. Kim, "Organic light-emitting diodes with 30% external quantum efficiency based on a horizontally oriented emitter," Adv. Funct. Mater. **23**, 3896–3900 (2013).

26. C. Mayr, S. Y. Lee, T. D. Schmidt, T. Yasuda, C. Adachi, and W. Brütting, "Efficiency enhancement of organic light-emitting diodes incorporating a highly oriented thermally activated delayed fluorescence emitter," Adv. Funct. Mater. **24**, 5232–5239 (2014).

27. T. Lampe, T. D. Schmidt, M. J. Jurow, P. I. Djurovich, M. E. Thompson, and W. Brütting, "Dependence of phosphorescent emitter orientation on deposition technique in doped organic films," Chem. Mater. **28**, 712–715 (2016).

28. M. J. Jurow, C. Mayr, T. D. Schmidt, T. Lampe, P. I. Djurovich, W. Brütting, and M. E. Thompson, "Understanding and predicting the orientation of heteroleptic phosphors in organic light-emitting materials," Nat. Mater. **15**, 85–91 (2016).

29. H. Mizuno, T. Maeda, H. Yanagi, H. Katsuki, M. Aresti, F. Quochi, M. Saba, A. Mura, G. Bongiovanni, F. Sasaki, and S. Hotta, "Optically pumped lasing from single crystals of a cyano-substituted thiophene/phenylene co-oligomer," Adv. Opt. Mater. **2**, 529–534 (2014).

30. H. Mizuno, T. Maeda, H. Yanagi, H. Katsuki, M. Aresti, F. Quochi, M. Saba, A. Mura, G. Bongiovanni, F. Sasaki, and S. Hotta, "Synthesis of thiophene/phenylene co-oligomers. V [1]. Functionalization at molecular terminals toward optoelectronic device applications," J. Heterocycl. Chem. **44**, 853–862 (2007).

31. S. Hotta and M. Goto, "Crystal structure analysis of 2,5-Bis(4-biphenylyl)thiophene," Adv. Mater. **14**, 498–501 (2002).

32. K. Hashimoto, F. Sasaki, S. Hotta, and H. Yanagi, "Amplified emission and field-effect transistor characteristics of one-dimensionally structured 2,5-Bis(4-biphenylyl)thiophene crystals," J. Nanosci. Nanotechnol. **16**, 3200–3205 (2016).

33. K. Bando, S. Kumeta, F. Sasaki, and S. Hotta, "Energy dispersions of anisotropic refractive indices of thiophene/phenylene co-oligomer crystals," Jpn. J. Appl. Phys. **50**, 101603 (2011).

34. H. H. Fang, Q. D. Chen, J. Yang, H. Xia, Y. G. Ma, H. Y. Wang, and H. B. Sun, "Two-photon excited highly polarized and directional upconversion emission from slab organic crystals," Opt. Lett. **35**, 441–443 (2010).

35. R. Ding, M. H. An, J. Feng, and H. B. Sun, "Organic single-crystalline semiconductors for light-emitting applications: recent advances and developments," Laser Photon. Rev. **13**, 1900009 (2019).

36. R. Ding, X. P. Wang, J. Feng, X. B. Li, F. X. Dong, W. Q. Tian, J. R. Du, H. H. Fang, H. Y. Wang, T. Yamao, S. Hotta, and H. B. Sun, "Clarification of the molecular doping mechanism in organic single-crystalline semiconductors and their application in color-tunable light-emitting devices," Adv. Mater. **30**, 1801078 (2018).

37. R. Ding, F. X. Dong, M. H. An, X. P. Wang, M. R. Wang, X. B. Li, J. Feng, and H. B. Sun, "High-color-rendering and high-efficiency white organic light-emitting devices based on double-doped organic single crystals," Adv. Funct. Mater. **29**, 1807606 (2019).

38. M. H. An, R. Ding, Q. C. Zhu, G. D. Ye, H. Wang, M. X. Du, S. N. Chen, Y. Liu, M. L. Xu, T. Xu, W. Wang, J. Feng, and H. B. Sun, "Well-balanced ambipolar organic single crystals toward highly efficient light-emitting devices," Adv. Funct. Mater. **30**, 2002422 (2020).

39. A. Rogac, "Towards next generation white LEDs: optics-electronics synergistic effect in a single-layer heterophase halide perovskite," Light Sci. Appl. **10**, 46 (2021).

40. Q. S. Shan, C. T. Wei, Y. Jiang, J. Z. Song, Y. S. Zou, L. M. Xu, T. Fang, T. T. Wang, Y. H. Dong, J. X. Liu, B. N. Han, F. J. Zhang, J. W. Chen, Y. J. Wang, and H. B. Zeng, "Perovskite light-emitting/detecting bifunctional fibres for wearable LiFi communication," Light Sci. Appl. **9**, 163 (2020).

41. L. Yang, F. Cai, Y. Yan, J. Li, D. Liu, A. J. Pearson, and T. Wang, "Conjugated small molecule for efficient hole transport in high-performance p-i-n type perovskite solar cells," Adv. Funct. Mater. **27**, 1702613 (2017).

42. Y. F. Miao, L. Cheng, W. Zou, L. H. Gu, J. Zhang, Q. Guo, Q. M. Peng, M. M. Xu, Y. R. He, S. T. Zhang, Y. Cao, R. Z. Li, N. N. Wang, W. Huang, and J. P. Wang, "Microcavity top-emission perovskite light-emitting diodes," Light Sci. Appl. **9**, 89 (2020).

43. L. Zhang, "High-performance quasi-2D perovskite light-emitting diodes: from materials to devices," Light Sci. Appl. **10**, 61 (2021).

44. H. Cho, J. Chung, J. Song, J. Lee, H. Lee, J. Lee, J. Moon, S. Yoo, and N. S. Cho, "Importance of Purcell factor for optimizing structure of organic light-emitting diodes," Opt. Express **27**, 11057–11068 (2019).

45. X. W. Chen, W. C. H. Choy, and C. J. Liang, "Modifications of the exciton lifetime and internal quantum efficiency for organic light-emitting devices with a weak/strong microcavity," Appl. Phys. Lett. **91**, 221112 (2007).

46. A. Salehi, X. Fu, D. H. Shin, and F. So, "Recent advances in OLED optical design," Adv. Funct. Mater. **29**, 1808803 (2019).

47. K. A. Neyts, "Simulation of light emission from thin-film microcavities," J. Opt. Soc. Am. **15**, 962–971 (1998).

48. T. Yamao, Y. Taniguchi, K. Yamamoto, T. Miki, S. Ota, S. Hotta, M. Goto, and R. Azumi, "Anisotropic refractive indices of organic crystals of thiophene/phenylene co-oligomers determined by microspectroscopic measurements," Jpn. J. Appl. Phys. **46**, 7478–7482 (2007).

49. T. Yamao, K. Yamamotoy, T. Inoue, Y. Okuda, Y. Taniguchiz, and S. Hotta, "Refractive index along the molecular long axis of an orthorhombic thiophene/phenylene co-oligomer crystal," Jpn. J. Appl. Phys. **48**, 04C174 (2009).

50. T. Yamao, N. Sakamoto, S. Hotta, H. Mizuno, and H. Yanagi, "Refractive index measurements of well-defined polygon crystals of thiophene/phenylene co oligomers," Jpn. J. Appl. Phys. **51**, 11PD03 (2012).

51. T. Yamao, K. Yamamoto, Y. Taniguchi, T. Miki, and S. Hotta, "Laser oscillation in a highly anisotropic organic crystal with a refractive index of 4.0," J. Appl. Phys. **103**, 093115 (2008).

52. F. S. Yi, Y. G. Bi, X. L. Zhang, D. Yin, Y. F. Liu, J. Feng, and H. B. Sun, "Highly flexible and mechanically robust ultrathin Au grid as electrodes for flexible organic light-emitting devices," IEEE Trans. Nanotechnol. **18**, 776–780 (2019).

53. S. X. Li, H. Xia, G. P. Zhang, X. L. Xu, Y. Yang, G. Wang, and H. B. Sun, "Shape-designable and size-tunable organic–inorganic hybrid perovskite micro-ring resonator arrays," Adv. Mater. Technol. **5**, 2000051 (2020).